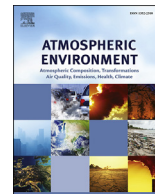




Contents lists available at ScienceDirect

# Atmospheric Environment

journal homepage: [www.elsevier.com/locate/atmosenv](http://www.elsevier.com/locate/atmosenv)

## Observation and simulation study of atmospheric aerosol nonsphericity over the Loess Plateau in northwest China



Pengfei Tian<sup>a</sup>, Xianjie Cao<sup>a</sup>, Lei Zhang<sup>a,\*</sup>, Hongbin Wang<sup>b</sup>, Jinsen Shi<sup>a</sup>,  
Zhongwei Huang<sup>a</sup>, Tian Zhou<sup>a</sup>, Hui Liu<sup>a</sup>

<sup>a</sup> Key Laboratory for Semi-Arid Climate Change of the Ministry of Education, College of Atmospheric Sciences, Lanzhou University, Lanzhou 730000, China

<sup>b</sup> Key Laboratory for Aerosol-Cloud-Precipitation of China Meteorological Administration, Nanjing University of Information Science and Technology, Nanjing 210044, China

### HIGHLIGHTS

- Aerosol aspect ratio (AR) was obtained from observations and numerical simulations.
- Aerosol nonsphericity varied by season with a pronounced maximum in the spring.
- The retrieved aerosol ARs ranged from 1.00 to 1.30 and peaked at about 1.06.
- AR parameterization provided a better shape input for aerosol optical modeling.
- Depolarization ratio decreased with increasing precipitable water in summer.

### ARTICLE INFO

#### Article history:

Received 8 February 2015

Received in revised form

9 July 2015

Accepted 13 July 2015

Available online 14 July 2015

#### Keywords:

Aerosol nonsphericity

SACOL

Lidar

Depolarization ratio

Aspect ratio

Precipitable water

### ABSTRACT

Aerosol nonsphericity, which is not well depicted in model calculations, seriously affects aerosol optical properties and subsequently alters the radiative forcing of the earth–atmosphere system. Based on aerosol backscattering linear depolarization ratio data observed by a polarization lidar at the Semi-Arid Climate and Environment Observatory of Lanzhou University (SACOL) from September 2009 to August 2012 and numerical computations, the spatial and temporal distribution of the aerosol depolarization ratio, parameterization of the derived aspect ratio and influence of water vapor on aerosol nonsphericity were investigated. Aerosol nonsphericity varied considerably by season, with a pronounced maximum in the spring, when more nonspherical aerosols were transported upward to the free troposphere; moreover, the column-averaged lidar depolarization ratios were 0.13, 0.09, 0.08 and 0.10 for the spring, summer, autumn and winter, respectively. The derived aerosol aspect ratio, a simplified parameter that describes the particle nonsphericity, ranged from 1.00 to 1.30 and peaked at approximately 1.06. A modified log-normal function, which was fitted to the frequency distribution of the derived aspect ratios, yielded a log-normal distribution parameterization for this parameter and provided a better shape input for the aerosol optical modeling. The monthly averaged aspect ratios reached a maximum of 1.13 during the spring and a minimum of 1.04 in autumn. The depolarization ratios decreased significantly with column-integrated increasing precipitable water in summer when there was sufficient precipitable water.

© 2015 Elsevier Ltd. All rights reserved.

### 1. Introduction

Aerosols are a primary component of the atmosphere and directly affect the radiative budget of the earth–atmosphere

system by scattering and absorbing solar radiation and by absorbing and emitting infrared radiation. They alter the optical properties and lifetime of clouds and the fraction of cloud cover by acting as cloud condensation nuclei or ice nuclei (Rosenfeld et al., 2014). In addition, they play a role in atmospheric heterogeneous interactions (Kolb and Worsnop, 2012). However, both direct radiative forcing and radiative forcing induced through aerosol–cloud interactions suffer from significant uncertainties. As

\* Corresponding author.

E-mail address: [zhanglei@lzu.edu.cn](mailto:zhanglei@lzu.edu.cn) (L. Zhang).

indicated by the fifth assessment report of the Intergovernmental Panel on Climate Change (IPCC), the effective radiative forcing of the former ranges from  $-0.95$  to  $+0.05$   $\text{Wm}^{-2}$ , whereas that of the latter ranges from  $-1.2$  to  $0.0$   $\text{Wm}^{-2}$  (Myhre et al., 2013). Thus, further research should combine field observations, laboratory studies of aerosol chemistry and physical properties, and model simulations in order to better understand the role that aerosols play in the earth–atmosphere system (Prather et al., 2008).

The shape of aerosols is a key factor that affects their optical properties and radiative effects (Dubovik et al., 2006; Adachi and Buseck, 2015). Although the assumption of a simplified spherical shape allows for the calculation of aerosol optical and radiative properties by the Lorenz–Mie theory (Wiscombe, 1980; Ricchiuzzi et al., 1998), mineral dust (Kandler et al., 2009), dry sea salt (Chamaillard et al., 2003) and aggregated soot particles (Li et al., 2003) always exhibit complex and apparent nonspherical shapes. The impact of the particle shape on single scattering optical properties, such as the asymmetry parameter and single scattering albedo, may be small (Yang et al., 2007; Otto et al., 2011), but it is larger on polarimetric optical properties (Müller et al., 2010, 2012). Thus, for nonspherical conditions, the assumption of a simplified spherical shape will cause large differences in optical property calculations (Lenoble et al., 2013) and great uncertainties in radiative forcing simulations (Kahnert et al., 2007; Yi et al., 2011). Nevertheless, the current aerosol models cannot include global aerosol shape inputs due to the lack of a global data set for atmospheric aerosol characteristics, especially for nonspherical aerosols such as dust (Durant et al., 2009). Neglecting particle nonsphericity may underestimate the aerosol optical depth (AOD) by as much as 20% when the AOD is greater than 1 (Feng et al., 2009). Recent research indicates that adding a nonspherical parameter in the aerosol clustering process leads to a 16% change in the total reflectance and up to a 100% change in the polarized reflectance at the top of the atmosphere (Chen et al., 2015).

The aspect ratio (AR) and lidar backscattering depolarization ratio are two prime parameters that represent the nonsphericity of particles. There are two commonly used definitions for the lidar backscattering depolarization ratio: the linear and circular backscattering depolarization ratios that can be obtained from observations by different lidar systems. The aspect ratio of a spheroid is defined as the ratio between the major and the minor axes (Mishchenko and Travis, 1998). Aerosol aspect ratios can be obtained by electron-microscope observations (Okada et al., 2001; Reid et al., 2003; Chou et al., 2008) or by the optical retrieval approach. The measured aspect ratio originates primarily from dry particles, which is the main limitation of electron-microscope observations (Kandler et al., 2011; Titos et al., 2014). Though Saharan dust particles are always hydrophobic (Kaaften et al., 2009), aerosol hygroscopicity heavily influences the aerosol optical properties of other particle types. The scattering enhancement factors are up to 2.2 and 1.8 for marine and anthropogenic aerosols when the relative humidity is 80% (Titos et al., 2014). Water-soluble deliquescence particles, such as NaCl and  $(\text{NH}_4)_2\text{SO}_4$ , exist as crystalline solids with high depolarization ratios below the efflorescence point and exist as solution droplets with low depolarization ratios above the deliquescence point. These particles gradually change phase according to the relative humidity between the efflorescence and deliquescence points (Tang and Munkelwitz, 1994; Sakai et al., 2000); thus, the particle depolarization ratio decreases with increasing water vapor in the atmosphere.

Aspect ratios measured at a low relative humidity differ greatly from those measured at ambient atmospheric conditions and therefore cannot be used directly to assess the radiative budget of the earth–atmosphere system (Zieger et al., 2013). Optical retrieval of the aerosol aspect ratio is based on observed optical parameters

under ambient conditions. Kocifaj et al. (2008) simultaneously measured the phase function and extinction coefficient near the ground and interpreted the two parameters in terms of the surface distribution function and mean effective aspect ratio for aerosol particles and, thus, arrived at the aerosol aspect ratio with a retrieval approach. The advantage of the optical retrieval approach, despite its approximation and simplification, lies in the fact that it deals with real aerosol particles that exist in ambient atmospheric conditions.

The T-matrix is an efficient approach to study the optical properties of rotationally symmetric, nonspherical (for example, spheroid) particles (Liou, 2002). This approach was initially introduced by Waterman (1971) and was then developed by Mishchenko and Travis (1998); it is now widely applied in the field of light scattering and related fields (Mishchenko et al., 2014). As an example, Wiegner et al. (2009) simulated Saharan dust aerosols by applying the T-matrix approach. To reduce the computation time, kernel look-up tables created by Dubovik et al. (2006) were used to retrieve the aerosol aspect ratios in this research.

Aerosol nonsphericity over SACOL was investigated based on observations from a depolarization lidar, a sun photometer, and a simulation of T-matrix and an improved geometric optics approach. Section 2 introduces the data and methodology. The spatial and temporal distributions of the aerosol depolarization ratio are discussed in section 3. The frequency distribution of the derived aerosol aspect ratio and its parameterization are presented in section 4.1. The annual variation of the aerosol nonsphericity is presented in section 4.2, and the influence of water vapor on the aerosol nonsphericity is discussed in section 5.

## 2. Data and methodology

### 2.1. Observation site

The Semi-Arid Climate and Environment Observatory of Lanzhou University (SACOL, 35.946° N, 104.137° E, and 1965.8 m ASL) is located in the semi-arid region of the Loess Plateau in northwest China, approximately 48 km from the center of Lanzhou City (Huang et al., 2008a). Because SACOL is located in the downstream region of the Taklamakan and Gobi deserts (Huang et al., 2008b), it is always affected by desert dust, especially in the spring (Ling et al., 2014). Aerosols over SACOL exhibited their relatively strongest scattering (with the largest real part of the refractive indices) and weakest absorption (with the lowest imaginary part of the refractive indices) during the spring (Bi et al., 2011). More detailed information is provided in the literature by Huang et al. (2008a).

SACOL is an international research observatory that consists of a large set of advanced instruments. It is a member of the Aerosol Robotic Network (AERONET) (Holben et al., 1998), NASA Micro-Pulse Lidar Network (MPLNET), Asian Dust and aerosol lidar observation Network (AD-Net), and the China Lidar Network (CLN). Observational and inversion data from an L2S-SM polarization lidar (Shimizu et al., 2004) and a sun photometer were used in this research.

### 2.2. Sun photometer data

The raw data collected using the sun photometer over SACOL were processed by the AERONET program (Dubovik and King, 2000), which yielded a set of aerosol optical and microphysical parameters that included AOD, size distribution, refractive indices (real part  $R_{ref}$  and imaginary part  $I_{ref}$ ), effective radius ( $r_{eff}$ ), single scattering albedo ( $SSA$ ), fine mode fraction ( $FMF$ ), surface albedo at different wavelengths and so on. Precipitable water, the total water vapor in the column, was retrieved from the observation at the

935 nm channel of the sun photometer. It was used to analyze the influence of water vapor on the aerosol nonsphericity (Section 5).

The cloud-screened and quality-assured level 2.0 product from AERONET from September 2009 to August 2012 was utilized in this research. To coordinate with the sun photometer and lidar data, parameters at 440 nm and 675 nm wavelengths were linearly interpolated to yield those at 532 nm. The volume size distribution and the refractive indices serve as input parameters for the numerical calculations.

### 2.3. Lidar data and preprocessing

The dual-wavelength depolarization lidar data from September 2009 to August 2012, comprising 833 complete observation days, were utilized in this research. The lidar was designed to acquire vertical profiles of the aerosol backscattering intensity at 532 nm and 1064 nm and the backscattering linear depolarization ratio at 532 nm. The backscattering linear depolarization ratio  $\delta_{linear}$  is defined as

$$\delta_{linear} = P_{\perp}(\pi) / P_{\parallel}(\pi), \quad (1)$$

where  $P_{\perp}(\pi)$  and  $P_{\parallel}(\pi)$  are the measured perpendicular and parallel backscatter intensities, respectively. The depolarization ratio for spherical particles is 0, and nonspherical aerosols have higher linear depolarization ratios.

The vertical resolution of the L2S-SM lidar is 6 m, and it acquires one vertical profile every 15 min. Because lidar signals are always contaminated by sunlight, dark-current noise and thermal noise from the optical system, the lidar data were denoised by using an automatic denoising method (Tian et al., 2014). Multiple scattering effect in our lidar observations was ignored, because multiple scattering from aerosol particles should be taken into account only for a space-borne lidar geometry (very large observed volume) and particles with effective radii larger than 3  $\mu\text{m}$  (Wandinger et al., 2010). To match the lidar data with the sun photometer data, we selected two lidar profiles with times that were closest to those of the specified sun photometer data, obtaining 642 pairs of matched lidar and sun photometer data.

The signal-to-noise ratio (SNR) of the depolarization ratio increased with increasing height. Though the overlap of the telescope was compensated below 600 m (Shimizu et al., 2004), lidar signals near the surface showed considerable instability. Therefore, each lidar profile was averaged from 0.12 to 8.0 km above the ground with SNR greater than 1 to derive the column-averaged depolarization ratio  $\delta_{averaged}$ :

$$\delta_{averaged} = \int_{0.12}^{8.0} \delta(h) dh / \int_{0.12}^{8.0} dh, \quad (2)$$

where  $h$  is the vertical height and  $\delta(h)$  is the corresponding depolarization ratio.

The normalized frequency distribution (NFD) of the depolarization ratio was defined to clearly depict the characteristics of aerosol depolarization ratio. The depolarization ratio value, ranging from 0 to 0.5, was divided into 50 bins, and the heights were also divided by a vertical resolution of 6 m. The frequency distribution ( $FD(\delta, h)$ ) is defined as a function of depolarization ratio and the vertical height:

$$FD(\delta, h) = \text{count}(\delta_i \leq \delta \leq \delta_{i+1}, h = h_j), \quad (3)$$

where  $\delta_i$  is the depolarization ratio in the  $i$ th depolarization ratio

bin,  $h_j$  is the height in the  $j$ th height bin, and  $FD(\delta, h)$  is the depolarization ratio count confined to the  $i$ th depolarization ratio bin and  $j$ th height bin. The frequency distribution ( $FD(\delta, h)$ ) was then normalized by its maximum value ( $\max(FD)$ ) to obtain the normalized frequency distribution ( $NFD(\delta, h)$ ):

$$NFD(\delta, h) = FD(\delta, h) / \max(FD). \quad (4)$$

### 2.4. Numerical computation of aerosol nonsphericity

T-matrix is a basic method to represent particle nonsphericity. Mishchenko and Travis (1998) discussed in detail the application of the T-matrix approach, including its capabilities and limitations.

The outputs of the T-matrix code include the extinction and scattering cross sections and the scattering matrix. The dimensionless scattering matrix for randomly oriented, rotationally symmetric, independently nonspherical scattering particles is defined as follows (Mishchenko et al., 2002):

$$F(\theta) = \begin{bmatrix} a_1(\theta) & b_1(\theta) & 0 & 0 \\ b_1(\theta) & a_2(\theta) & 0 & 0 \\ 0 & 0 & a_3(\theta) & b_2(\theta) \\ 0 & 0 & -b_2(\theta) & a_4(\theta) \end{bmatrix}, \quad (5)$$

where  $\theta$  is the scattering angle with the laser propagating direction set to  $\theta = 0$  and the backscattering direction set to  $\theta = \pi$ . The backscattering linear depolarization ratio is derived as follows (Mishchenko and Hovenier, 1995):

$$\delta_{linear} = [a_1(\pi) + a_3(\pi)] / [a_1(\pi) - a_3(\pi)]. \quad (6)$$

We obtained the simulated depolarization ratio ( $\delta_{simulated}$ ) with equation (6). The depolarization ratio increased monotonically with an increase of the aspect ratio, and this was especially true when the aspect ratio ranged from 1.00 to 2.00 (Fig. 1).

In numerical computations, however, the T-matrix method is not applicable to large particles with extreme aspect ratios (i.e., largely elongated or oblated spheroids) because of numerical instability. Specifically, for small and moderate size parameters, the T-matrix method (Mishchenko and Travis, 1998) was used, whereas the improved geometric optics method (Yang and Liou, 1996) was used for large size parameters (Dubovik et al., 2006; Yang et al., 2007; Ge et al., 2011). Look-up tables are simulated in the

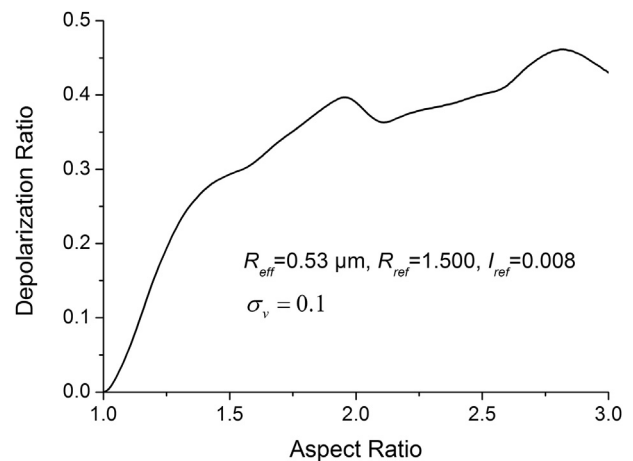


**Fig. 1.** T-matrix simulated depolarization ratio as a function of aspect ratio. The numerical calculations were conducted with an aspect ratio step of 0.01 from 1.00 to 3.00, with the input parameters effective radius ( $R_{eff}$ ) and refractive indices (real part  $R_{ref}$  and imaginary part  $I_{ref}$ ) set to the average values of the AERONET products and the standard deviation ( $\sigma_v$ ) set to 0.1.

numerical integration of spheroid optical properties over size and shape (Dubovik et al., 2006) for reducing the computation time. Such look-up tables and the software package from Dubovik et al. (2006) were used in the forward numerical computations in this research (Fig. 2).

The retrieval of the aspect ratio is summarized in the flowchart in Fig. 2. The volume aerosol size distribution and refractive indices provided by AERONET serve as inputs to the numerical computations. We used the lognormal function to generate axial ratio distributions similar to those in the literature (Dubovik et al., 2006). Such axial ratio distributions with an equal presence of prolate and oblate spheroids with the same aspect ratios were used to run the forward calculations. The output scattering matrix was used to calculate the simulated depolarization ratio (equation (6)). The integral averaging of the axial ratio distribution was set to the derived aerosol aspect ratio ( $AR_{Eff}$ ) when the simulated depolarization ratio ( $\delta_{simulated}$ ) most closely matched the column-averaged lidar depolarization ratio ( $\delta_{observed}$ ). The numerical computations were conducted by a 0.01 step of the integral averaging of the axial ratio distribution from 1.00 to 3.00.

### 3. Aerosol depolarization ratio from the lidar observations

As depicted in Fig. 3 (a), the aerosol depolarization ratio generally decreased with increasing height. The average depolarization ratio profile of each season was greater than 0.10 near the ground, and it decreased to less than 0.04 at a height of 6 km. The relatively slow decrease of the depolarization ratio from 1 to 2 km was due to the inhibition of vertical mixing by the boundary layer top. The depolarization ratio profile in the spring (MAM in Fig. 3 (a)) had the largest value. The depolarization ratio profiles in the summer and autumn similarly decreased with increasing height, and there was little difference in their values within the boundary layer. Because of the strong thermodynamics in the summer, more nonspherical aerosols were transported to higher altitudes; therefore, the depolarization ratio at the free troposphere in the summer was higher than that in the autumn.

The column-averaged depolarization ratio in the spring, which is the season with the greatest dust loading, was obviously higher than that in the other seasons (Fig. 3 (b)). It had a similar frequency distribution in the summer and autumn. The averages of the column-averaged depolarization ratio in the spring, summer, autumn, and winter were 0.13, 0.09, 0.08, and 0.10, respectively.

The normalized frequency distribution (NFD) of the lidar-observed depolarization ratios from September 2009 to August 2012, which comprised 833 complete observation days, is presented in Fig. 4. The NFD of depolarization ratios is described by three main characteristics: (1) the maximum NFD decreased with

increasing height, indicating that nonspherical aerosols were generated at the surface and that the sphericity decreased as aerosols were transported upward; (2) the small NFD near zero at the bottom–left corner of each season was due to highly nonspherical aerosols with high depolarization ratios within the atmospheric boundary layer; and (3) the top-right corner of each season, where the depolarization ratios were greater than 0.3, represents clouds.

The spring season experienced a much larger NFD range of values greater than 0.4 (green, yellow and red in Fig. 5) than in the other seasons; this indicates that more nonspherical aerosols were transported upward to the free troposphere during the spring. The smallest range of NFD value greater than 0.4, which occurred in the autumn, was due to the smallest amount of nonspherical aerosols in this season. Small-value NFD ranges (the bottom–left corner) existed in all seasons.

### 4. Derived aerosol aspect ratios from numerical computations

#### 4.1. Parameterization of the derived aerosol aspect ratios

The 642 matched pairs of sun photometer and lidar data from September 2009 to August 2012 were utilized to retrieve the aerosol aspect ratios, as shown in the flowchart in Fig. 2. The derived aspect ratios ranged from 1.00 to 1.30 and were much lower than the results from the electron-microscopic single-particle analyses (Okada et al., 2001; Reid et al., 2003; Chou et al., 2008; Kandler et al., 2011). The frequency distribution is similar to a log-normal distribution and peaked at approximately 1.06 (Fig. 6), which was lower than that found by Kocifaj et al. (2008). This was because Kocifaj et al. (2008) researched aerosol aspect ratios just near the ground, while in this research, the total column-averaged atmospheric aerosols were considered. The results of Kocifaj et al. (2008) showed that more than 80% of Viennese aerosols had aspect ratios less than 1.4 and that all the aspect ratios were less than 2.0. Even Asian dust can be simulated with a mean aspect ratio of 1.25 (Huang et al., 2015).

The frequency distribution of the derived aspect ratios was parameterized by a modified log-normal distribution function (Kandler et al., 2009):

$$h(AR) = \frac{1}{\sqrt{2\pi}\sigma(AR-1)} \exp\left[-\frac{1}{2}\left(\frac{\ln(AR-1)-\mu}{\sigma}\right)^2\right], \quad (7)$$

where AR is the derived aspect ratio and  $h(AR)$  is the power density as a function of the derived aspect ratio. Because the current aerosol models, especially the dust-cycle models, cannot depict aerosol

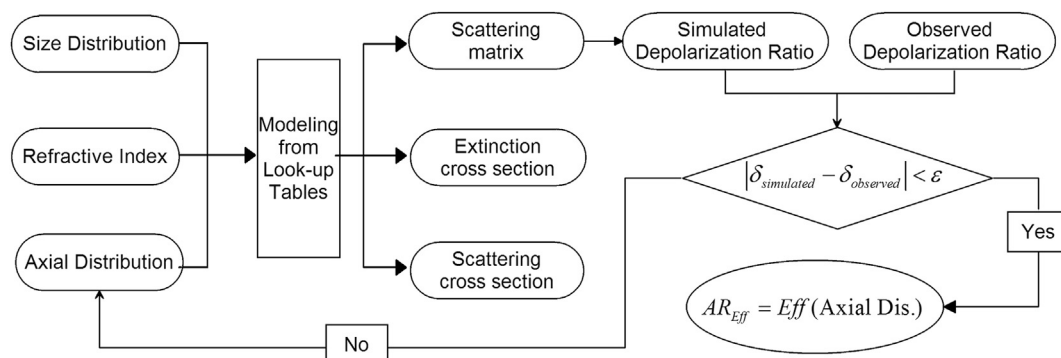


Fig. 2. Flowchart for aspect ratio retrieval based on optical observations and numerical simulation.

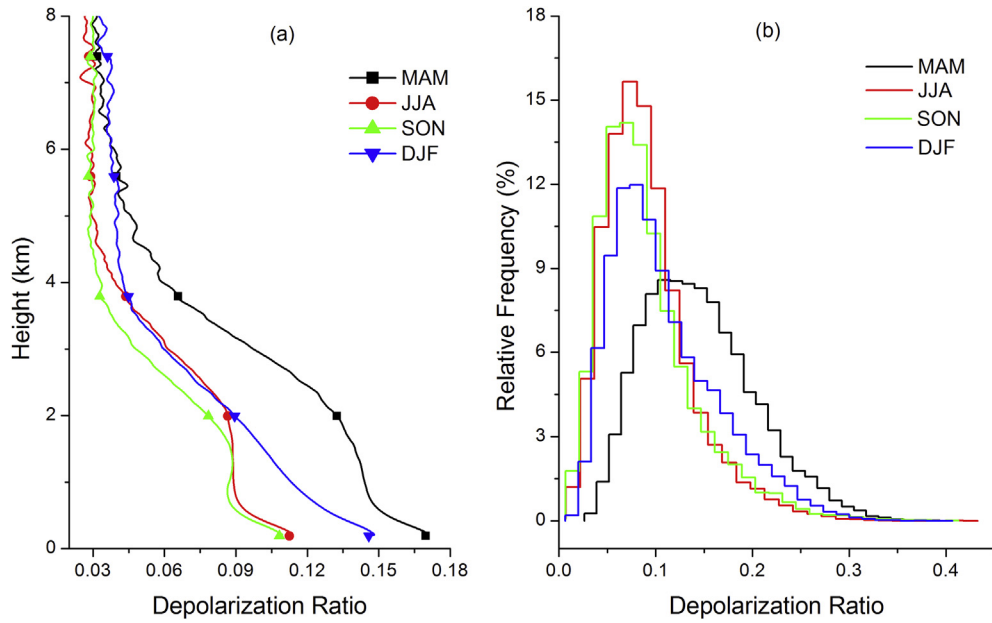


Fig. 3. (a) Vertical profiles of the aerosol depolarization ratio and (b) frequency distribution of the column averaged depolarization ratio in four seasons.

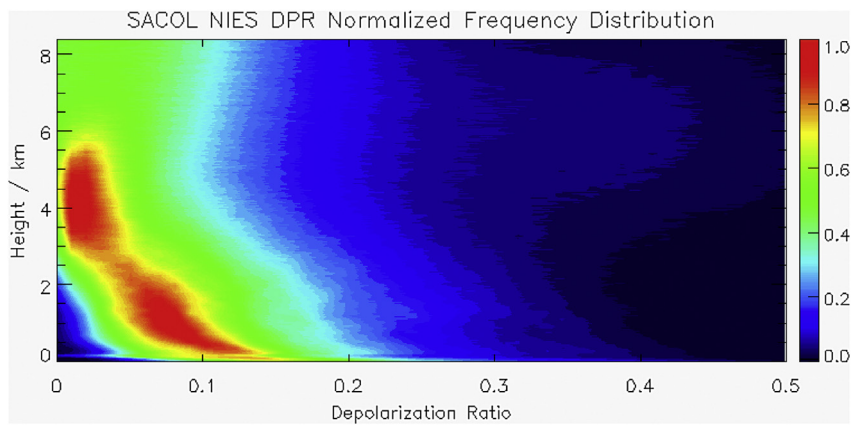


Fig. 4. Normalized frequency distribution of the lidar observed depolarization ratios.

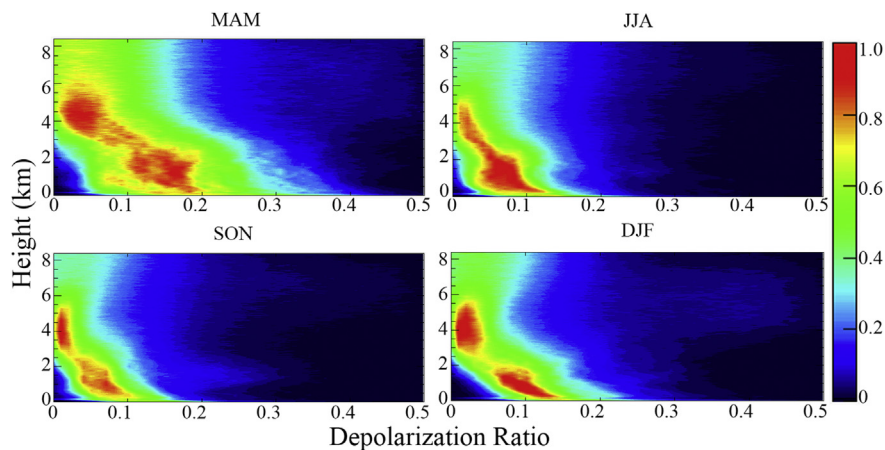
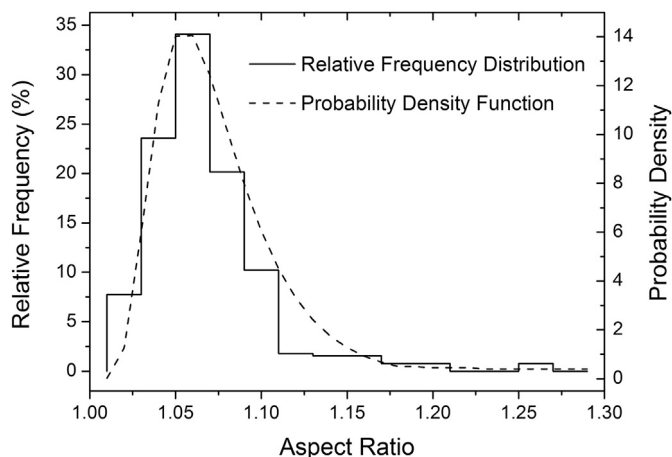


Fig. 5. Seasonal NFD variation of the lidar observed depolarization ratios.



**Fig. 6.** Frequency distribution and probability density function of the derived aspect ratios. The vertical step line depicts the frequency distribution of the retrieved aspect ratios. The parameterized probability density function is depicted by the dashed line, with distribution parameters  $\sigma = 0.4574$  and  $\mu = -2.6939$  (equation (7)).

shape very well (Durant et al., 2009), the derived aspect ratios provided a better shape input for aerosol optical modeling. Furthermore, unlike the aspect ratios measured by an electron-microscope, the aspect ratios derived in this research were based on optical observations of the ambient atmosphere and, thus, can directly serve as model inputs. Because the column-averaging smoothes the information of possibly more than one aerosol type at different heights to a column value, this work is only valid to some extent.

4.2. Annual variation of aerosol nonsphericity

The annual variations of some monthly averaged aerosol parameters are presented in Fig. 7. The monthly averaged depolarization ratio and the derived aspect ratio reached their maximum during the spring and minimum in autumn. The higher

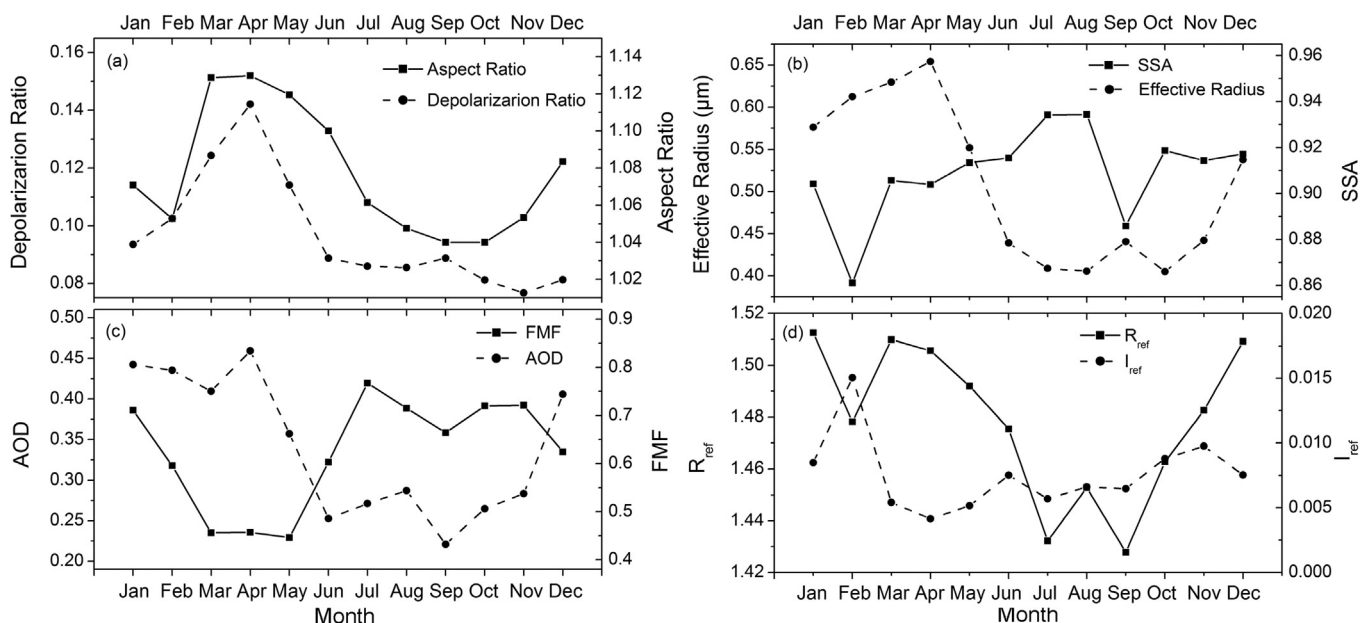


**Fig. 7.** Annual variations of the aerosol parameters: (a) derived aspect ratio and depolarization ratio; (b) effective radius and single scattering albedo (SSA); (c) aerosol optical depth (AOD) and fine-mode fraction (FMF); and (d) real and imaginary parts of the refractive indices.

**Table 1**  
SSA, imaginary part of the refractive indices and surface albedo in February calculated from available records from AERONET. Parameters without the subscript '2012' represent the years 2010 and 2011.

Parameter	SSA	SSA <sub>2012</sub>	$I_{ref}$	$I_{ref,2012}$	Albedo	Albedo <sub>2012</sub>
Avg.	0.92	0.84	0.006	0.019	0.15	0.70
Std.	0.03	0.03	0.004	0.006	0.01	0.24
Sample size	28	58	28	58	97	74

depolarization ratios and the derived aspect ratios during the spring were caused by dry dust aerosols, while the smaller ones were due to the moist, anthropogenic pollutants. A maximum of depolarization ratios was also found at Nagoya in spring, when aerosols were transported from the Asian continent (Sakai et al., 2000).

Furthermore, the single scattering albedo (SSA) reached its minimum of 0.86 in February. This SSA minimum was mainly contributed by the extreme minimum SSA in February 2012 (Table 1) when the imaginary part of the refractive indices was very large. The fine-mode fraction maximum and effective radius minimum also supported the conclusion that the SSA minimum in February was caused by fine particles with extremely large absorptions. In fact, the surface albedo in February was much higher in 2012 than that in 2010 and 2011 because there was more snowfall in February 2012. And there was no dust event in February 2012 according to the weather records. The higher albedo increases aerosol absorption because absorbing aerosols absorb not just the downward solar radiation but also the reflected upward radiation (Chul, 2012).

5. Influence of water vapor on aerosol nonsphericity

By modifying the shape and size distribution of the aerosols, water vapor alters the aerosol optical properties (Titos et al., 2014). Therefore, the variation of the column-averaged depolarization ratio as a function of column-integrated atmospheric precipitable water was investigated.

Precipitable water exhibited considerable seasonal variations with a pronounced summer maximum and winter minimum. It was mostly less than 0.5 cm in spring and reached 2.5 cm in autumn. The depolarization ratio had an apparent dependency on precipitable water in summer when there was sufficient precipitable water (Fig. 8). Sakai et al. (2000) studied the aerosol depolarization ratios in summer in the 2–4 km height region and noted that high depolarization ratios were found only where the relative humidity was less than 50% and the maximum of depolarization ratios decreased with increasing relative humidity. They also found low depolarization ratios with low water vapor during the winter, which agrees with the result in this study.

The relationship between the aerosol depolarization ratio and precipitable water was studied in detail. The depolarization ratio significantly decreased with increasing precipitable water in summer, as illustrated in Fig. 9. The linear fitting results showed a significant decreasing trend (Sig. = 0.000) of the depolarization ratio with increasing precipitable water; moreover, the precipitable water explained 80.8% of the variation in the averaged depolarization ratio ( $R^2 = 0.808$ ) in summer when there was ample precipitable water. As explained in section 1, a decrease in aerosol nonsphericity with increasing water vapor is a typical behavior of hygroscopic growth. In the case studies of Granados-Muñoz et al. (2015), the lidar observed depolarization ratio decreased with increasing relative humidity.

## 6. Conclusions

Aerosol shape is a major parameter that seriously affects aerosol optical properties and radiative forcing. Aerosol nonsphericity was investigated based on three years of depolarization lidar and sun photometer observations over the Semi-Arid Climate and Environment Observatory of Lanzhou University (SACOL) and numerical computations. The main conclusions are summarized as follows:

- (1) The aerosol depolarization ratios decreased with increasing height. Aerosol nonsphericity exhibited considerable seasonal variations with a pronounced maximum in spring, when more nonspherical aerosols were transported upward to the free troposphere. The column-averaged lidar depolarization ratios were 0.13, 0.09, 0.08, and 0.10 in the spring, summer, autumn and winter, respectively.

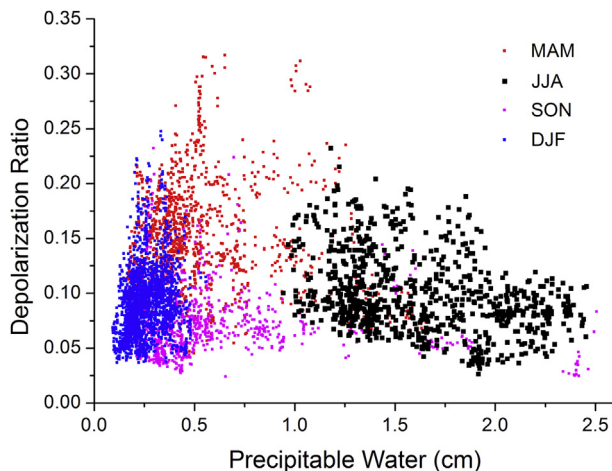


Fig. 8. The column-averaged aerosol depolarization ratio as a function of column-integrated atmospheric precipitable water.

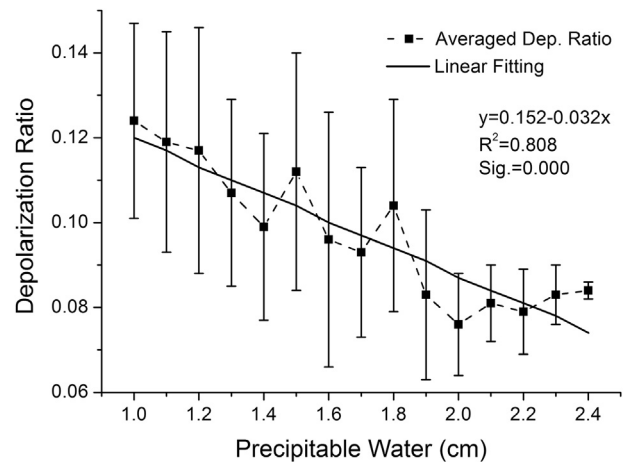


Fig. 9. Relationship between the depolarization ratio and the precipitable water in summer, with precipitable water divided into 15 bins, each spanning a width of 0.1 cm, from 1.0 to 2.4 cm. The squares indicate averages, and the bars represent standard deviation for each bin. The solid line is the linear fitting of the averaged depolarization ratio.

- (2) Aerosol aspect ratios were derived by combining the lidar-observed depolarization ratios and numerical computations. The derived aspect ratios ranged from 1.00 to 1.30, and the frequency distribution was akin to a log-normal distribution that peaked at approximately 1.06. A modified log-normal function was fitted to the frequency distribution of the derived aspect ratios, thus yielding a log-normal distribution parameterization of the derived aspect ratio with the distribution parameters  $\sigma = 0.4574$  and  $\mu = -2.6939$ . Unlike the aspect ratios measured using an electron-microscope, the aspect ratios derived in this research were based on optical observations of the ambient atmosphere, which provided a better shape input for aerosol optical modeling. The results in this work are only valid to some extent because the column-averaging smoothes the information of possibly more than one aerosol type at different heights to a column value.
- (3) When the precipitable water was quite small, there was no obvious dependency between the aerosol depolarization ratio and precipitable water. However, in summer, when there was sufficient precipitable water, there was a significant decreasing trend of the depolarization ratio with increasing precipitable water. Moreover, the precipitable water explained 80.8% of the variation in the averaged depolarization ratio ( $R^2 = 0.808$ ) in summer.

## Acknowledgments

This research is supported by the National Basic Research Program of China (2012CB955302), the National Natural Science Foundation of China (41205112 and 41225018) and the Key Laboratory for Aerosol-Cloud-Precipitation of China Meteorological Administration (KDW1303). We acknowledge the Semi-Arid Climate and Environment Observatory of Lanzhou University (SACOL) for providing the lidar data. We acknowledge SACOL and the Aerosol Robotic Network (AERONET) for providing the sun photometer data. We thank the well-respected Oleg Dubovik, Tatsiana Lapionak and Michael I. Mishchenko for providing numerical computation codes, the kernel look-up tables and kind instructions. The two anonymous reviewers are gratefully acknowledged for their detailed and helpful comments.

## References

- Adachi, K., Buseck, P.R., 2015. Changes in shape and composition of sea-salt particles upon aging in an urban atmosphere. *Atmos. Environ.* 100, 1–9.
- Bi, J., Huang, J., Fu, Q., Wang, X., Shi, J., Zhang, W., Huang, Z., Zhang, B., 2011. Toward characterization of the aerosol optical properties over Loess Plateau of North-western China. *J. Quant. Spectrosc. Radiat. Transf.* 112, 346–360.
- Chamaillard, K., Jennings, S.G., Kleefeld, C., Ceburnis, D., Yoon, Y.J., 2003. Light backscattering and scattering by nonspherical sea-salt aerosols. *J. Quant. Spectrosc. Radiat. Transf.* 79, 577–597.
- Chen, H., Cheng, T., Gu, X., Wu, Y., 2015. Impact of particle nonsphericity on the development and properties of aerosol models for East Asia. *Atmos. Environ.* 101, 246–256.
- Chou, C., Formenti, P., Maille, M., Ausset, P., Helas, G., Harrison, M., Osborne, S., 2008. Size distribution, shape, and composition of mineral dust aerosols collected during the African monsoon multidisciplinary analysis special observation period 0: dust and biomass-burning experiment field campaign in Niger, January 2006. *J. Geophys. Res. Atmos.* 113, D00C10.
- Chul, E.C., 2012. In: Dr Abdul-Razzak, Hayder (Ed.), *Aerosol Direct Radiative Forcing: a Review, Atmospheric Aerosols - Regional Characteristics - Chemistry and Physics*. InTech, ISBN 978-953-51-0728-6. <http://dx.doi.org/10.5772/50248>.
- Dubovik, O., King, M.D., 2000. A flexible inversion algorithm for retrieval of aerosol optical properties from Sun and sky radiance measurements. *J. Geophys. Res. Atmos.* 105, 20673–20696.
- Dubovik, O., Sinyuk, A., Lapyonok, T., Holben, B.N., Mishchenko, M., Yang, P., Eck, T.F., Volten, H., Muñoz, O., Veihelmann, B., van der Zande, W.J., Leon, J.F., Sorokin, M., Slutsker, I., 2006. Application of spheroidal models to account for aerosol particle nonsphericity in remote sensing of desert dust. *J. Geophys. Res. Atmos.* 111, D11208.
- Durant, A.J., Harrison, S.P., Watson, I.M., Balkanski, Y., 2009. Sensitivity of direct radiative forcing by mineral dust to particle characteristics. *Prog. Phys. Geogr.* 33, 80–102.
- Feng, Q., Yang, P., Kattawar, G.W., Hsu, C.N., Tsay, S.C., Laszlo, I., 2009. Effects of particle nonsphericity and radiation polarization on retrieving dust properties from MODIS observations. *J. Aerosol Sci.* 40, 776–789.
- Ge, J.M., Su, J., Fu, Q., Ackerman, T.P., Huang, J.P., 2011. Dust aerosol forward scattering effects on ground-based aerosol optical depth retrievals. *J. Quant. Spectrosc. Radiat. Transf.* 112, 310–319.
- Granados-Munoz, M.J., Navas-Guzman, F., Bravo-Aranda, J.A., Guerrero-Rascado, J.L., Lyamani, H., Valenzuela, A., Titos, G., Fernandez-Galvez, J., Alados-Arboledas, L., 2015. Hygroscopic growth of atmospheric aerosol particles based on active remote sensing and radiosounding measurements: selected cases in south-eastern Spain. *Atmos. Meas. Tech.* 8, 705–718.
- Holben, B., Eck, T., Slutsker, I., Tanre, D., Buis, J., Setzer, A., Vermote, E., Reagan, J., Kaufman, Y., Nakajima, T., 1998. AERONET-A federated instrument network and data archive for aerosol characterization. *Remote Sens. Environ.* 66, 1–16.
- Huang, J.P., Zhang, W., Zuo, J.Q., Bi, J.R., Shi, J.S., Wang, X., Chang, Z.L., Huang, Z.W., Yang, S., Zhang, B.D., Wang, G.Y., Feng, G.H., Yuan, J.Y., Zhang, L., Zuo, H.C., Wang, S.G., Fu, C.B., Chou, J.F., 2008a. An overview of the semi-arid climate and environment research observatory over the Loess Plateau. *Adv. Atmos. Sci.* 25, 906–921.
- Huang, J., Minnis, P., Chen, B., Huang, Z.W., Liu, Z.Y., Zhao, Q.Y., Yi, Y.H., Ayers, J.K., 2008b. Long-range transport and vertical structure of Asian dust from CALIPSO and surface measurements during PACDEX. *J. Geophys. Res. Atmos.* 113, D23212.
- Huang, X., Yang, P., Kattawar, G., Liou, K.N., 2015. Effect of mineral dust aerosol aspect ratio on polarized reflectance. *J. Quant. Spectrosc. Radiat. Transf.* 151, 97–109.
- Kaaden, N., Massling, A., Schladitz, A., Müller, T., Kandler, K., Schutz, L., Weinzierl, B., Petzold, A., Tesche, M., Leinert, S., Deutscher, C., Ebert, M., Weinbruch, S., Wiedensohler, A., 2009. State of mixing, shape factor, number size distribution, and hygroscopic growth of the Saharan anthropogenic and mineral dust aerosol at Tinfou, Morocco. *Tellus B* 61, 51–63.
- Kahnert, M., Nousiainen, T., Raisanen, P., 2007. Mie simulations as an error source in mineral aerosol radiative forcing calculations. *Q. J. R. Meteorol. Soc.* 133, 299–307.
- Kandler, K., Schutz, L., Deutscher, C., Ebert, M., Hofmann, H., Jäckel, S., Jaenicke, R., Knippertz, P., Lieke, K., Massling, A., Petzold, A., Schladitz, A., Weinzierl, B., Wiedensohler, A., Zorn, S., Weinbruch, S., 2009. Size distribution, mass concentration, chemical and mineralogical composition and derived optical parameters of the boundary layer aerosol at Tinfou, Morocco, during SAMUM 2006. *Tellus B* 61, 32–50.
- Kandler, K., Lieke, K., Benker, N., Emmel, C., Kupper, M., Müller-Ebert, D., Ebert, M., Scheuvs, D., Schladitz, A., Schutz, L., Weinbruch, S., 2011. Electron microscopy of particles collected at Praia, Cape Verde, during the Saharan Mineral Dust Experiment: particle chemistry, shape, mixing state and complex refractive index. *Tellus B* 63, 475–496.
- Kocifaj, M., Horvath, H., Gangl, M., 2008. Retrieval of aerosol aspect ratio from optical measurements in Vienna. *Atmos. Environ.* 42, 2582–2592.
- Kolb, C.E., Worsnop, D.R., 2012. Chemistry and composition of atmospheric aerosol particles. *Annu. Rev. Phys. Chem.* 63, 471–491.
- Lenoble, J., Mishchenko, M., Herman, M., 2013. Absorption and scattering by molecules and particles. In: Lenoble, J., Remer, L., Tanre, D. (Eds.), *Aerosol Remote Sensing*. Springer, Berlin Heidelberg, pp. 13–51.
- Li, J., Anderson, J.R., Buseck, P.R., 2003. TEM study of aerosol particles from clean and polluted marine boundary layers over the North Atlantic. *J. Geophys. Res. Atmos.* 108 (D6), 4189.
- Ling, X.L., Guo, W.D., Fu, C.B., 2014. Composite analysis of impacts of dust aerosols on surface atmospheric variables and energy budgets in a semiarid region of China. *J. Geophys. Res. Atmos.* 119, 3107–3123.
- Liou, K.N., 2002. *An Introduction to Atmospheric Radiation*, second ed. Academic Press, New York.
- Mishchenko, M.I., Hovenier, J.W., 1995. Depolarization of light backscattered by randomly oriented nonspherical particles. *Opt. Lett.* 20, 1356–1358.
- Mishchenko, M.I., Travis, L.D., 1998. Capabilities and limitations of a current FORTRAN implementation of the T-matrix method for randomly oriented, rotationally symmetric scatterers. *J. Quant. Spectrosc. Radiat. Transf.* 60, 309–324.
- Mishchenko, M.I., Travis, L.D., Lacis, A.A., 2002. *Scattering, Absorption and Emission of Light by Small Particles*. Cambridge University Press, Cambridge.
- Mishchenko, M.I., Zakharova, N.T., Khlebtsov, N.G., Wriedt, T., Videen, G., 2014. Comprehensive thematic T-matrix reference database: a 2013–2014 update. *J. Quant. Spectrosc. Radiat. Transf.* 146, 349–354.
- Müller, D., Weinzierl, B., Petzold, A., Kandler, K., Ansmann, A., Müller, T., Tesche, M., Freudenthaler, V., Esselborn, M., Heese, B., Althausen, D., Schladitz, A., Otto, S., Knippertz, P., 2010. Mineral dust observed with AERONET Sun photometer, Raman lidar, and in situ instruments during SAMUM 2006: shape-independent particle properties. *J. Geophys. Res. Atmos.* 115.
- Müller, D., Lee, K.H., Gasteiger, J., Tesche, M., Weinzierl, B., Kandler, K., Müller, T., Toledano, C., Otto, S., Althausen, D., Ansmann, A., 2012. Comparison of optical and microphysical properties of pure Saharan mineral dust observed with AERONET Sun photometer, Raman lidar, and in situ instruments during SAMUM 2006. *J. Geophys. Res. Atmos.* 117.
- Myhre, G., Shindell, D., Bréon, F.M., Collins, W., Fuglestad, J., Huang, J., Koch, D., Lamarque, J.F., Lee, D., Mendoza, B., Nakajima, T., Robock, A., Stephens, G., Takemura, T., Zhang, H., 2013. Anthropogenic and natural radiative forcing. In: Stocker, T.F., Qin, D., Plattner, G.-K., Tignor, M., Allen, S.K., Boschung, J., Nauels, A., Xia, Y., Bex, V., Midgley, P.M. (Eds.), *Climate Change 2013: The Physical Science Basis. Contribution of Working Group I to the Fifth Assessment Report of the Intergovernmental Panel on Climate Change*. Cambridge University Press, Cambridge.
- Okada, K., Heintzenberg, J., Kai, K.J., Qin, Y., 2001. Shape of atmospheric mineral particles collected in three Chinese arid-regions. *Geophys. Res. Lett.* 28, 3123–3126.
- Otto, S., Trautmann, T., Wendisch, M., 2011. On realistic size equivalence and shape of spheroidal Saharan mineral dust particles applied in solar and thermal radiative transfer calculations. *Atmos. Chem. Phys.* 11, 4469–4490.
- Prather, K.A., Hatch, C.D., Grassian, V.H., 2008. Analysis of atmospheric aerosols. *Annu. Rev. Anal. Chem.* 1, 485–514.
- Reid, E.A., Reid, J.S., Meier, M.M., Dunlap, M.R., Cliff, S.S., Broumas, A., Perry, K., Maring, H., 2003. Characterization of African dust transported to Puerto Rico by individual particle and size segregated bulk analysis. *J. Geophys. Res. Atmos.* 108 (D19), 8591.
- Ricchiazzi, P., Yang, S.R., Gautier, C., Sowle, D., 1998. SBDART: a research and teaching software tool for plane-parallel radiative transfer in the Earth's atmosphere. *Bull. Am. Meteorol. Soc.* 79, 2101–2114.
- Rosenfeld, D., Sherwood, S., Wood, R., Donner, L., 2014. Climate effects of aerosol-cloud interactions. *Science* 343, 379–380.
- Sakai, T., Shibata, T., Kwon, S.A., Kim, Y.S., Tamura, K., Iwasaka, Y., 2000. Free tropospheric aerosol backscatter, depolarization ratio, and relative humidity measured with the Raman lidar at Nagoya in 1994–1997: contributions of aerosols from the Asian Continent and the Pacific Ocean. *Atmos. Environ.* 34, 431–442.
- Shimizu, A., Sugimoto, N., Matsui, I., Arao, K., Uno, I., Murayama, T., Kagawa, N., Aoki, K., Uchiyama, A., Yamazaki, A., 2004. Continuous observations of Asian dust and other aerosols by polarization lidars in China and Japan during ACE-Asia. *J. Geophys. Res. Atmos.* 109, D19517.
- Tang, I.N., Munkelwitz, H.R., 1994. Water activities, densities, and refractive-indexes of aqueous sulfates and sodium-nitrate droplets of atmospheric importance. *J. Geophys. Res. Atmos.* 99, 18801–18808.
- Tian, P., Cao, X., Liang, J., Zhang, L., Yi, N., Wang, L., Cheng, X., 2014. Improved empirical mode decomposition based denoising method for lidar signals. *Opt. Commun.* 325, 54–59.
- Titos, G., Jefferson, A., Sheridan, P.J., Andrews, E., Lyamani, H., Alados-Arboledas, L., Ogren, J.A., 2014. Aerosol light-scattering enhancement due to water uptake during the TCAP campaign. *Atmos. Chem. Phys.* 14, 7031–7043.
- Wandinger, U., Tesche, M., Seifert, P., Ansmann, A., Müller, D., Althausen, D., 2010. Size matters: influence of multiple scattering on CALIPSO light-extinction profiling in desert dust. *Geophys. Res. Lett.* 37, L10801. <http://dx.doi.org/10.1029/2010GL042815>.
- Waterman, P., 1971. Symmetry, unitarity, and geometry in electromagnetic scattering. *Phys. Rev. D* 3, 825.
- Wiegner, M., Gasteiger, J., Kandler, K., Weinzierl, B., Rasp, K., Esselborn, M., Freudenthaler, V., Heese, B., Toledano, C., Tesche, M., Althausen, D., 2009. Numerical simulations of optical properties of Saharan dust aerosols with emphasis on lidar applications. *Tellus B* 61, 180–194.
- Wiscombe, W.J., 1980. Improved Mie scattering algorithms. *Appl. Opt.* 19, 1505–1509.
- Yang, P., Feng, Q., Hong, G., Kattawar, G.W., Wiscombe, W.J., Mishchenko, M.I., Dubovik, O., Laszlo, I., Sokolik, I.N., 2007. Modeling of the scattering and radiative properties of nonspherical dust particles. *J. Aerosol Sci.* 38, 995–1014.
- Yang, P., Liou, K.N., 1996. Geometric-optics-integral-equation method for light scattering by nonspherical ice crystals. *Appl. Opt.* 35, 6568–6584.
- Yi, B.Q., Hsu, C.N., Yang, P., Tsay, S.C., 2011. Radiative transfer simulation of dust-like aerosols: uncertainties from particle shape and refractive index. *J. Aerosol Sci.* 42, 631–644.
- Zieger, P., Fierz-Schmidhauser, R., Weingartner, E., Baltensperger, U., 2013. Effects of relative humidity on aerosol light scattering: results from different European sites. *Atmos. Chem. Phys.* 13, 10609–10631.